JOURNAL OF SPACECRAFT AND ROCKETS
Vol. 30, No. 6, November–December 1993

Supersonic/Hypersonic Flowfield Predictions over Typical Finned Missile Configurations

Bilal A. Bhutta* and Clark H. Lewis†
VRA, Inc., Blacksburg, Virginia 24063

Continuing developments in high-speed finned-missile technology require new accurate and computationally fast numerical techniques for predicting the associated viscous flows at small-to-moderate angles of attack over a wide range of low-to-high Mach numbers (3–15). In this study, a three-dimensional parabolized Navier-Stokes scheme has been developed using a general real-gas flux-vector-splitting technique based on the van Leer approach. Three types of flux-vector-differencing approaches are considered, and their numerical stability and accuracy characteristics are investigated. Results show that a hybrid approach, using first-order full upwinding across the embedded shock and central differencing otherwise, produces an oscillation-free shock front, while it is also strongly convergent and accurate in the near-wall region. This hybrid approach is used to predict Mach 3 and 15 flows over a typical finned-missile configuration at 25,000 ft altitude using perfect-gas and equilibrium-air gas models. Angles of attack of 0, 2, and 5 deg are considered, and fin-thickness and fin-deflection effects are investigated. Fin-deflection studies indicate that, for such high-speed missiles, even small amounts off in deflection can substantially modify the vehicle's aerodynamics.

Nomenclature

CA = axial-force coefficient
CM = pitching-moment coefficient (with respect to the nose)
CN = normal-force coefficient
f = convective flux vector in ξ_i direction
h = static enthalpy, ft^2/s^2
J = determinant of the transformation Jacobian
L = reference length for force and moment coefficients, ft
M = Mach number
P, p = static pressure, lbf/ft^2
P_w = wall pressure, lbf/ft^2
$PINF$ = freestream pressure, p_∞, lbf/ft^2
Q_w = wall heat transfer rate, Btu/ft^2/s
q = vector of flowfield unknowns
R_b = local body radius, ft
Re = Reynolds number, $(\rho VRn)/\mu$
RN, Rn = nose radius, ft
s = viscous flux vector in ξ_i direction
T = static temperature, °R
$TINF$ = freestream static temperature, T_∞, °R
U_j = contravariant velocity in the x_j direction, $\xi_{j,x_k}u_k$,1/s
u = x component of local velocity, ft/s
u_j = u, v, and w, respectively, for $j = 1$, 2, and 3, ft/s
V = total velocity, ft/s
v = y component of local velocity, ft/s
w = z component of local velocity, ft/s
X, x = coordinate along body axis, ft
X_{CP} = axial location of the center of pressure, ft
x_j = x, y, and z, respectively, for $j = 1$, 2, and 3, ft
Z^* = real-gas coefficient
α = angle of attack, deg
γ = specific-heat ratio
ε = M_∞/Re_∞
μ = viscosity, lbf-s/ft^2
ξ_1 = marching or streamwise coordinate
ξ_2 = coordinate measured from the body to the outer bow shock
ξ_3 = coordinate measured from the windward to the leeward pitch plane
ρ = static density, slug/ft^3
ϕ = circumferential angle measured from the windward side, deg

Subscripts
j, k = indicial notation representing 1, 2, and 3
s = shock quantity
w = wall quantity
$'$ = partial derivative
∞ = freestream quantity

Superscript
T = vector or matrix transpose

Received Oct. 22, 1992; revision received Jan. 1, 1993; accepted for publication Jan. 25, 1993.

*Vice President. Senior Member AIAA.
†President. Associate Fellow AIAA.

I. Introduction

RECENT developments in strategic as well as theater missile defense (TMD) systems have put increased emphasis on small, smart, and highly maneuverable high-speed (supersonic/hypersonic) missiles and kinetic-kill interceptor configurations. The recently announced Theater High-Altitude Area Defense (THAAD) initiative by the Strategic Defense Command (SDC) is an example of such interest. There are also several other technology programs being actively sponsored by the Strategic Defense Initiative Office (SDIO) that are directed toward the development of similar advanced high-speed missile concepts (e.g., the ENDO-LEAP program, the D2 program, etc.).[1,2] Such high-speed missile configurations typically involve complicated control fins and represent a challenge from a computational aerothermodynamics point of view. Many of the smart missiles are also being designed with accurate aero-optical seekers and homing devices,[2,3] and due to the very high operating speeds, the margin of error in vehicle performance is very small. Accurate and reliable design and operation of these high-speed missiles require an accurate knowledge of the surrounding viscous flowfield.

Classical missile aerodynamics has mainly dealt with relatively low-speed (subsonic to transonic) flows and, thus, has typically emphasized inviscid analyses augmented by empirical data to estimate control effectiveness. However, under the supersonic/hypersonic conditions of interest (Mach 3–15), viscous effects are important and play a significant role in determining the missile aerodynamics and aerothermodynamics. The aerothermodynamical aspects of the flow (such as air chemistry, surface heating, etc.)

are very important from an aero-optical viewpoint.[3] The mission importance of such missiles dictates accuracy of the supporting numerical aerothermodynamic predictions, and the realistic needs of a design and analysis procedure require a relatively fast turnaround. Thus, current technology directions show the need for developing accurate and computationally fast numerical techniques for predicting viscous flows over missile configurations with fins and control surface deflections.

The existing viscous schemes for predicting hypersonic external flows over three-dimensional geometries consist of Navier-Stokes (NS) schemes,[4,5] parabolized Navier-Stokes (PNS) schemes,[6–8] and viscous shock-layer (VSL) schemes.[9,10] The available NS schemes[4,5] are typically very time consuming and not well suited for typical design and analysis purposes. Over the years several new and robust three-dimensional PNS schemes[11–15] have been successfully developed for perfect-gas/equilibrium-air supersonic/hypersonic flows and have been used to predict flows over a wide range of geometry and flowfield conditions. Extensive comparisons of our three-dimensional PNS schemes have also been made with available wind-tunnel and flight experiments,[14,15] and the agreement has been very good.

To further enhance these three-dimensional PNS schemes to study various finned-missile configurations, in this study an approximate, general real-gas (nonequilibrium as well as equilibrium air) flux-vector-splitting (FVS) technique has been developed based on the van Leer flux-splitting approach.[16] This approximate real-gas flux-splitting scheme is simple and computationally efficient; however, it is also very accurate. Three types of flux-vector-differencing schemes are investigated in this study, and the results show that a hybrid approach provides the most suitable combination of stability and accuracy. This hybrid approach is then used to predict the flow over a typical missile configuration with four afterbody fins. Both perfect-gas and equilibrium-air predictions are made for 0-, 2-, and 5-deg angles of attack, and the effects of fin thickness and fin deflection are also investigated. It is assumed that the aft portions of the side fins could be deflected upward, and calculations are done with 0- and 5-deg deflection angles. The resulting predictions are compared with the undeflected case to show that fin deflection is a very powerful means of augmenting the aerodynamic characteristics of such high-speed missiles. In general, the results of these investigations are very promising and reflect the accuracy, efficiency, and robustness of the three-dimensional PNS approach developed in this study.

Solution Scheme

Coordinate System

The coordinate system used for the present three-dimensional PNS scheme is a general curvilinear coordinate system (ξ_1, ξ_2, ξ_3). Also, a body-fixed orthogonal (Cartesian) coordinate system is chosen such that the origin of the Cartesian coordinate system is at the tip of the blunt nose, and the x axis is aligned with the axis of the body. The ξ_1 coordinate is along the body and is also the marching direction. The ξ_2 coordinate stretches from the body to the outer bow shock and lies in an axis-normal plane, and the ξ_3 coordinate is measured in the crossflow direction from the windward pitch plane.

Governing Equations

The vector of unknowns consists of density ρ, the density-velocity products ρu, ρv, and ρw, the static temperature T, and the pressure p; i.e.,

$$\boldsymbol{q} = [\rho, \rho u, \rho v, \rho w, T, p]^T \tag{1}$$

The governing three-dimensional PNS equations are obtained from the full Navier-Stokes equations[17] written in general curvilinear coordinate system ξ_j, by neglecting the diffusion and dissipation effects in the ξ_1 direction. The five equations representing the differential conservation of mass, momentum, and energy are mathematically closed by using the equation of state for the gas mixture. For a perfect-gas model as well as an equilibrium-air gas model, this equation of state can be written in a nondimensional form as

$$\gamma_\infty p - Z^* \rho T = 0 \tag{2}$$

where $Z^* = 1$ for a perfect-gas model, and $Z^* = Z^*(p, T)$ for an equilibrium-air gas model. For the equilibrium-air case, the mixture thermodynamic and transport properties are provided in the form of a table based on the Miner-Blottner-Hansen data.[14,15] The equation of state and the five conservation equations can now be combined into the following vectorial equation:

$$\boldsymbol{f}_{1,\xi_1} + \boldsymbol{f}_{2,\xi_2} = \varepsilon\,(\boldsymbol{s}_{2,\xi_2} + \boldsymbol{s}_{3,\xi_3}) + \boldsymbol{h} \tag{3}$$

Real-Gas Flux-Splitting Approach

The basic flux-splitting technique used is based on the van Leer[16] approach, extended to three dimensions and a general curvilinear coordinate system. The resulting split flux vectors have the desirable feature of being continuously differentiable over the entire flow domain. The van Leer flux splitting was chosen because the resulting split flux vectors are continuous and differentiable across the sonic line, and the basic finite difference approach strongly requires continuously differentiable flux vectors. On the other hand, the Steger-Warming flux splitting[18] does not satisfy these continuity and differentiability requirements. In the present approximate real-gas flux-splitting approach, using the characteristic speed of sound of the real-gas mixture $[a(p, T)]$, two new thermodynamic state variables $\bar{\gamma}$ and $\bar{h}$ are defined as follows:

$$\bar{\gamma} = \bar{\gamma}(p,T) = \rho a^2/p \tag{4a}$$

$$\bar{h} = \bar{h}(p,T) = a^2/(\bar{\gamma} - 1) \tag{4b}$$

Using these definitions, we can now write the convective flux vectors as

$$\boldsymbol{f}_j(\boldsymbol{q}) = (\rho/J)\begin{bmatrix} U_j \\ uU_j + \xi_{j,x}a^2/\bar{\gamma} \\ vU_j + \xi_{j,y}a^2/\bar{\gamma} \\ wU_j + \xi_{j,z}a^2/\bar{\gamma} \\ [a^2/(\bar{\gamma}-1) + V^2/2]\,U_j \\ 0 \end{bmatrix} + (h - \bar{h})\begin{bmatrix} 0 \\ 0 \\ 0 \\ 0 \\ \rho U_j/J \\ 0 \end{bmatrix} \tag{5a}$$

or simply

$$\boldsymbol{f}_j = \boldsymbol{f}_{3j} + (h - \bar{h})\boldsymbol{f}_{1j} \tag{5b}$$

In a general real-gas case, $\bar{\gamma}$ and $\bar{h}$ are some unknown functions of p and T. Because of this implicit dependence of $\bar{\gamma}$ on p and T, the eigenvalues of the van Leer split fluxes of $\boldsymbol{f}_{3j}$ are no longer always of the same sign. In our approach we remove the effects of an implicit $\bar{\gamma}$ from $\boldsymbol{f}_{3j}$ by expanding it around an appropriately chosen distribution $\gamma^*(\xi_2, \xi_3)$; i.e.,

$$\boldsymbol{f}_j = \boldsymbol{f}_j^* + (\bar{\gamma} - \gamma^*)\boldsymbol{f}_{2j} + (h - \bar{h})\boldsymbol{f}_{3j} = \boldsymbol{f}_j^* + \tilde{\boldsymbol{f}}_j \tag{6}$$

Now the flux vector $\boldsymbol{f}_j^*$ has a form that fully satisfies all of the conditions of van Leer flux splitting and does not involve any eigenvalue problems. The flux vector $\tilde{\boldsymbol{f}}_j$ includes the effects of $(\bar{\gamma} - \gamma^*)$ differences and some additional real-gas effects given by the term $(h - \bar{h})$. The complete functional dependence of $\boldsymbol{f}_j$ on

the flowfield cannot be obtained in a closed form for a general real-gas case. Furthermore, it can have eigenvalues of a mixed nature due to the variable $\bar{\gamma}$ and $(h-\bar{h})$. For a general real gas, $\bar{f}_j$ can have eigenvalues of a mixed nature and, thus, cannot be safely differenced in a biased manner.

The approximate nature of this flux-splitting approach is only due to the approximate way in which the $\bar{f}_j$ terms are treated. Rather than find an exact and complicated splitting of the $\bar{f}_j$ terms, the approach used is first to minimize these terms and then to use accurate higher order differencing approximations to estimate them. This is done by using the fact that in almost all parabolic flows $\bar{\gamma}$ varies very slowly from one axial step to the next. Thus, by choosing the $\gamma^*(\xi_2, \xi_3)$ distribution at the current marching step to be the $\bar{\gamma}$ distribution from the previous marching step, the $(\bar{\gamma}-\gamma^*)$ differences are minimized. After having minimized $\bar{f}_j$ in this manner, second-order central-differenced approximations are used to approximate its spatial derivatives. It should be noted that in the perfect-gas limit $\bar{f}_j = 0$ and the flux splitting is exact.

Higher-Order Numerical Dissipation Effects

In this three-dimensional PNS approach, second-order central-differenced approximations are used for the ξ_2 and ξ_3 derivatives in the smooth (shock-free) flow regions,[14,15] and first-order backward-differenced approximations are used for the streamwise ξ_1 derivatives. To suppress any numerical oscillations caused by these difference approximations, fourth-order numerical dissipation effects are used in the axis-normal ξ_2 and crossflow ξ_3 directions, and for low Reynolds number flows, small amounts of second-order streamwise ξ_1 dissipation effects[14,15] are also included. However, across embedded shocks, only a first-order fully upwind formulation is used in the crossflow plane ($\xi_2\xi_3$ plane) because any higher order formulation, which involves information from the wrong side of the shock, results in numerical over- and undershoots in flowfield quantities across the shocks.

Bow Shock-Fitting and Predictor-Corrector Solution

After linearizing the governing PNS equations [Eqs. (3)] around the previous iteration,[11–15] the final differenced equations are written in a block-pentadiagonal form[12–15] that involves axis-normal ξ_2 and crossflow ξ_3 coupling terms. To properly treat these coupling effects, a predictor-corrector approach[12–15] is used that consists of three different steps: 1) the predictor step, 2) the shock solution, and 3) the corrector step. In the predictor step, the implicit crossflow coupling effects are neglected in favor of the axis-normal coupling effects.[12–15] Using the results of the predictor step at the shock, the crossflow-coupled differential shock-crossing equations are then solved to obtain the solution behind the shock.[12–14] This shock solution is then used to solve the corrector step. The corrector solution is then marched from the shock to the body using either plane-of-symmetry or periodic boundary conditions in the crossflow direction.[14,15] This overall iterative process is repeated until the solution converges at all grid points, and then the solution moves on to the next marching step. For some complicated three-dimensional flows, solution under-relaxation was also used to maintain solution convergence.[12–14]

Three Dimensional PNS Boundary Conditions

In the present study, only flows with a pitch plane of symmetry are considered, and the initial conditions to start the PNS solutions are obtained from an appropriate VSL blunt-body solution scheme.[9,10] The boundary conditions at the wall[11–15] consist of the equation of state for the gas, no-slip boundary conditions, specified wall-temperature distribution, and zero pressure derivative in the ξ_2 direction ($p_{\xi_2}=0$).

Elliptic Grid Generation and Related Considerations

The present elliptic grid-generation scheme is based on the work of Sorenson and Steger,[19] Chaussee and Steger,[20] and Kaul and Chaussee.[21] In this approach a grid is generated between the body and the outer bow shock, which corresponds to the solution of the two elliptic partial differential equations involving two forcing functions $P(\xi_2, \xi_3)$ and $R(\xi_2, \xi_3)$[14,19–21]:

$$\begin{aligned} a y_{\xi_3\xi_3} - 2b y_{\xi_3\xi_2} + c y_{\xi_2\xi_2} &= -J^2 P(\xi_2, \xi_3) \\ a z_{\xi_3\xi_3} - 2b z_{\xi_3\xi_2} + c z_{\xi_2\xi_2} &= -J^2 R(\xi_2, \xi_3) \end{aligned} \tag{7a}$$

where

$$\begin{aligned} a &= y_{\xi_2} y_{\xi_2} + z_{\xi_2} z_{\xi_2}, & c &= y_{\xi_3} y_{\xi_3} + z_{\xi_3} z_{\xi_3} \\ b &= y_{\xi_2} y_{\xi_3} + z_{\xi_2} z_{\xi_3}, & J &= y_{\xi_2} z_{\xi_3} - z_{\xi_3} z_{\xi_2} \end{aligned} \tag{7b}$$

The functions P and R in Eqs. (7) control the grid clustering and grid orthogonality. Numerically it is very difficult to exactly satisfy the user-specified grid-clustering distribution and also the orthogonality constraints of the elliptic grid (described by the P and R functions inside the wall-to-shock region). In the present approach (and also the approach used in Refs. 19–21), the P and R functions at the wall and at the shock are obtained using grid orthogonality constraints, whereas inside the shock layer they are exponentially varied from their specified values at the wall to their specified values at the shock. In our earlier high Mach number studies[14,15] and also in many other elliptic grid-generation studies,[8,19–21] the exponential distributions of P and R across the layer were obtained using the following power laws:

$$\begin{aligned} \mathcal{P}(\xi_2, \xi_3) &= [\omega_1(\xi_2)]\,[P_w(\xi_3)] + [\omega_2(\xi_2)]\,[P_s(\xi_3)] \\ \mathcal{R}(\xi_2, \xi_3) &= [\omega_1(\xi_2)]\,[R_w(\xi_3)] + [\omega_2(\xi_2)]\,[R_s(\xi_3)] \end{aligned} \tag{8a}$$

where

$$\begin{aligned} \omega_1(\xi_2) &= [(\xi_2 - 1)/(\mathrm{LMAX} - 1) - 1]^4 \\ \omega_2(\xi_2) &= [(\xi_2 - 1)/(\mathrm{LMAX} - 1)]^4 \end{aligned} \tag{8b}$$

and where $\xi_2 = 1$ at the wall and $\xi_2 = \mathrm{LMAX}$ at the shock. It will be shown later that for low Mach number (Mach 3) flows a power-of-10 variation rather than the power-of-4 variation in Eqs. (8) is more appropriate.

Classical elliptic grid-generation schemes[19–21] are very time consuming and costly; however, in this approach[14,15] significant computational speed was achieved by not requiring strict grid orthogonality and by requiring the shock boundary to move in the ξ_2 coordinate direction. Our earlier studies[14,15] have shown that this improved elliptic grid-generation approach only takes approximately 20% longer than the simplest cylindrical grid generation.

III. Results and Discussion

The numerical flux-splitting, shock-fitting, and grid-generation techniques described earlier were incorporated in a three-dimensional central-differenced-based perfect-gas/equilibrium-air PNS scheme[14,15] that was then used to do several calculations on a typical finned configuration. The results of these studies are summarized next.

Comparisons of Differencing Techniques

The effects of various differencing procedures used for estimating the axis-normal flux vector were investigated by considering the zero angle-of-attack flow over a 4/0/10/0 deg multiconic configuration. The nose radius Rn is 0.5 in. and each conical section is 25 Rn long. The flowfield conditions considered correspond to fully turbulent Mach 15 flow at an altitude of 25,000 ft (Table 1). The 10-deg flare was chosen because it produced a strong embedded shock without causing axial flow separation. Calculations were done using 1) a completely central-differenced approach, 2) a hybrid approach using fully upwind shock and central differencing in smooth shock-free regions, and 3) a third-order FVS approach with fully upwind shock. In all cases 150 grid points were used between the body and the shock, and the grid spacing at the wall was 1×10^{-3} percent of the local shock standoff distance. The accuracy of the central-differenced approach has already been

Table 1 Freestream conditions for cases 1–6

Quantity	
Mach no.	
Cases 1–4	15
Cases 5 and 6	3
Altitude, ft	25,000
Pressure, psf	780.72
Temperature, °R	425.59
Wall temperature, °R	1,000
Flow type	Turbulent
Angle of attack, deg	
Cases 1–4	0, 2, 5
Cases 5 and 6	0, 5

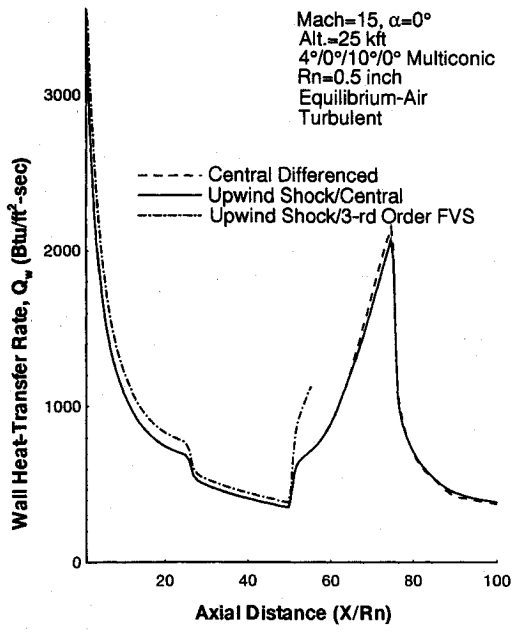

Fig. 1 Axial distribution of surface heat transfer rate for case 1.

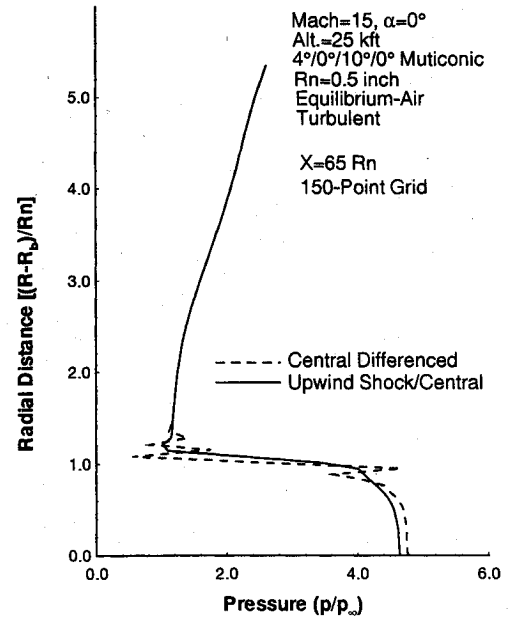

Fig. 2 Pressure profiles for case 1 at $x = 65\ Rn$.

demonstrated[14,15] and, thus, was used to judge the accuracy of the other two approaches, especially in the forebody region that is unaffected by the flare shock.

The predictions of the surface heat transfer rate for the three differencing strategies (Fig. 1) show that in the forebody region the completely central-differenced approach (case 1a) and the hybrid approach (case 1b) are the same, which should be the case because there are no embedded shocks. The predictions of the third-order FVS scheme (case 1c) in this region are, however, approximately 15% too high. Furthermore, the third-order FVS scheme failed to properly converge over the 10-deg flare region. In this study a diagonal-lumping approach was used for the third-order FVS scheme in which, instead of simply neglecting the two outermost off-diagonal terms of the implicit left-hand side (LHS), they were lumped onto the diagonal. Numerical tests showed that this resulted in better convergence than either a simple first-order one-sided differencing or the neglection of the off-diagonal terms.

The pressure profiles predicted at $x = 65\ Rn$ using the central-differenced approach (case 1a) and the hybrid approach (case 1b) are shown in Fig. 2. In this case, central differencing across the strong embedded shock results in severe numerical oscillations, which are as much as ±50% across the shock, and also appears to slightly overpredict the wall pressure (Fig. 2) and wall heat transfer rate (Fig. 1) in this region. This overprediction also results in a slightly higher drag force (Table 2). On the other hand, with upwinding across the shock, the shock is captured well and the predicted flowfield is oscillation free. Furthermore, the predicted shock front is quite sharp and not diffused. The computing times for these cases are shown in Table 3 and show that the central-differenced approach (case 1a) required 25 s on a Cray Y-MP, whereas the hybrid approach (case 1b) took only 28 s. Thus, it is clear that the hybrid approach of using first-order upwind differencing of the split fluxes across the shock and central differencing otherwise is a better approach because it provides stability, robustness, and accuracy while its additional computational expense is less than 10%.

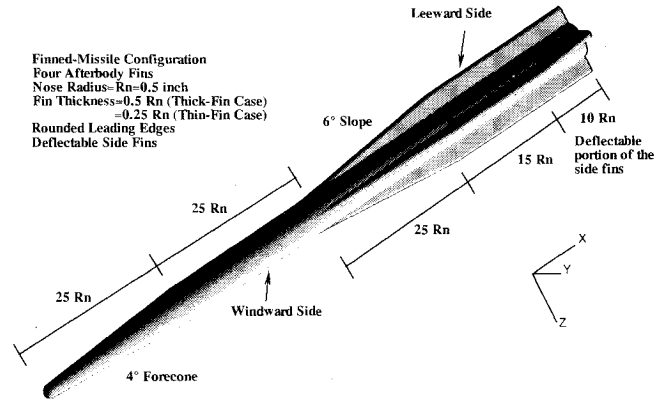

Fig. 3 Finned-missile configuration.

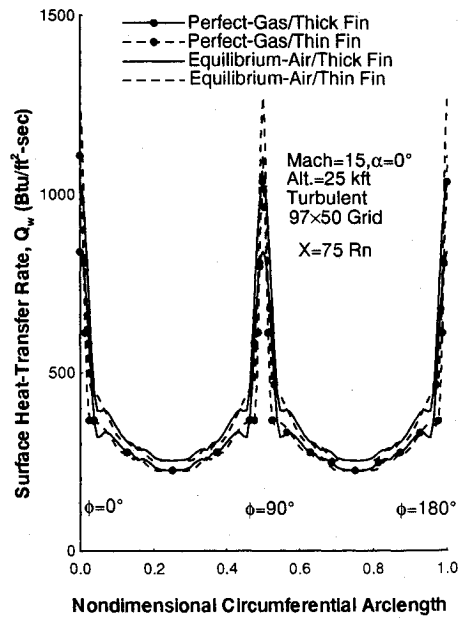

Fig. 4 Crossflow distribution of surface heat transfer rate for case 2 at $x = 75\ Rn$.

Table 2 Force and moment data for cases 1–6

Case	Fin type[a]	Angle of attack, deg	Gas model[b]	M_∞	CA[c]	CN[c]	$-CM$[c]	X_{CP}/L
1a	——	0	EQ	15	0.05141	——	——	——
1b	——	0	EQ	15	0.05038	——	——	——
2a	THK	0	PG	15	0.1645 [c]	——	——	——
2b	THN	0	PG	15	0.1589	——	——	——
2c	THK	0	EQ	15	0.172	——	——	——
2d	THN	0	EQ	15	0.1716	——	——	——
3a	THK	2	PG	15	0.1707	0.117	0.06892	0.5967
3b	THK	2	EQ	15	0.1766	0.1085	0.06435	0.5929
4a	THK	5	PG	15	0.1931	0.5103	0.3226	0.632
4b	THK	5	EQ	15	0.2039	0.51	0.3237	0.6347
5a	THK	0	PG	3	0.2701	——	——	——
5b	THK-D	0	PG	3	0.2846	−0.2105	−0.2004	0.9519
6a	THK	5	PG	3	0.2678	1.259	0.829	0.6587
6b	THK-D	5	PG	3	0.2718	1.062	0.642	0.6043

[a]THK=undeflected thick-fin case, THN=undeflected thin-fin case, and THK-D=deflected thick-fin case (5-deg fin deflection).
[b]EQ=equilibrium air; PG=perfect gas.
[c]Reference area and reference length L for these calculations are 22.58 Rn^2 and 100 Rn, respectively.

Table 3 Computing tmes and grids for cases 1–6

Case	Fin type[a]	Angle of attack, deg	Gas model[b]	M_∞	X/Rn from–to	Grid[c] $N3\times N2\times N1$	Time[d] m:s
1a	——	0	EQ	15	1–100	1 ×150 ×170	0:25
1b	——	0	EQ	15	1–100	1 ×150 ×170	0:28
2a	THK	0	PG	15	45–100	97 × 50 ×114	12:40
2b	THN	0	PG	15	45–100	97 × 50 ×145	15:50
2c	THK	0	EQ	15	45–100	97 × 50 ×114	11:58
2d	THN	0	EQ	15	45–100	97 × 50 ×129	14:21
3a	THK	2	PG	15	1–100	97 × 50 ×180	18:50
3b	THK	2	EQ	15	1–100	97 × 50 ×175	19:00
4a	THK	5	PG	15	1–100	97 × 50 ×187	20:03
4b	THK	5	EQ	15	1–100	97 × 50 ×174	22:19
5a	THK	0	PG	3	45–100	97 × 50 ×112	9:50
5b	THK-D	0	PG	3	90–100	97 × 50 × 21	2:31
6a	THK	5	PG	3	1–100	97 × 50 ×185	13:50
6b	THK-D	5	PG	3	90–100	97 × 50 × 21	1:42

[a]THK=undeflected thick-fin case, THN=undeflected thin-fin case, and THK-D=deflected thick-fin case (5-deg fin deflection).
[b]EQ=equilibrium air; PG=perfect gas.
[c]$N1$, $N2$, and $N3$ are the number of grid points in the streamwise, axis-normal, and crossflow directions, respectively.
[d]Computing times on Cray Y-MP with CFT77 compiler and autovectorization.

Finned-Missile Flowfield Calculations

The finned-missile configuration considered in this study is shown in Fig. 3 and consists of a sphere-cone-cylinder body with four symmetrical fins over the latter half of the body. The fin height is approximately equal to the body radius, Rn is 0.5 in., the overall body length is 50 in., and the aft 5-in. portion of the side fins is assumed to be deflectable. The freestream conditions considered consist of Mach 15 and 3 flows at an altitude of 25,000 ft (Table 1). Only fully turbulent conditions were considered, and the wall temperature is kept fixed at 1000°R. Mach 15 calculations (cases 2–4) were done at 0-, 2-, and 5-deg angles of attack with equilibrium-air as well as perfect-gas models. Mach 3 calculations (cases 5 and 6) were done at 0- and 5-deg angles of attack with only a perfect-gas model. The Mach 15 calculations (cases 2–4) were done using the undeflected fin configuration, whereas 0- and 5-deg deflection angles for side fins were considered under Mach 3 conditions (cases 5 and 6).

All calculations over the finned portion were done using 97 crossflow planes and 50 axis-normal grid points (97×50). The grid spacing at the wall was 1×10^{-3} percent of the local shock-standoff distance, and the grids were circumferentially clustered at the fin tips to provide a good representation of the fin leading edges. For the zero angle-of-attack calculations, the forebody calculations were done using a one-plane axisymmetric PNS solution that was then rotated slightly upstream of the fin location to provide the necessary 97×50 starting solution.

Mach 15 Calculations

For the zero angle-of-attack Mach 15 conditions, two types of undeflected-fin configurations were tested, viz.,1) a thick-fin configuration and 2) a thin-fin configuration. The thick-fin case had fins with leading-edge radius of 0.25 in. (0.5-in. thick fins), and the thin-fin case had a leading-edge radius of 0.125 in. (0.25-in. thick fins). Flowfields over both thick- and thin-fin configurations were computed at zero angle of attack using perfect-gas and equilibrium-air gas models. The circumferential distributions of the surface heat transfer rate at $x=75$ Rn (peak leading-edge heating region) for the various zero angle-of-attack calculations (cases 2a–2d) are shown in Fig. 4, which shows that the thinner fin produces approximately 15% higher leading-edge heating rate. In general, the thin-fin leading-edge heating rate is approximately 20% higher than the corresponding thick-fin case, and the equilibrium-air predictions are approximately 20% higher than the corresponding perfect-gas case (Figs. 4 and 5). Figure 6 shows that the equilibrium-air pressure predictions on the fins and bare body in the afterbody region are much lower than the perfect-gas predictions, and the thinner fin results in about 10% lower leading-edge pressure. However, due to the small fin tip area and a cylindrical body, these pressure differences do not substantially affect the overall drag. The drag predictions for these cases are shown in Table 2 and show that the thin-fin case has approximately 4% less drag than the thick-fin case. The equilibrium-air gas model predicts approximately 5% higher drag than the perfect-gas model mainly due to the larger forebody drag for the equilibrium-air case.

Calculations for the thick-fin case were also done at 2- and 5-deg angles of attack. Figure 7 shows a sample of the computational grids generated at the body end ($x=100$ Rn) for the 5-deg angle-of-attack case. The force and moment data at the body end for these calculations (Table 2) show a large increase in the normal force and pitching moment due to the fins. With increasing angle

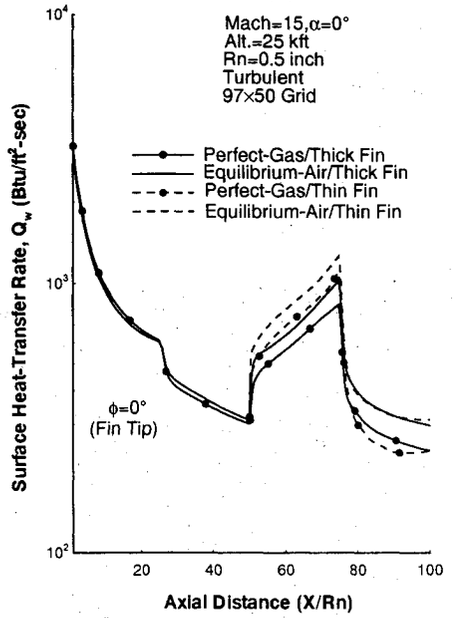

Fig. 5 Axial distribution of surface heat transfer rate for case 2 along $\phi = 0$ deg.

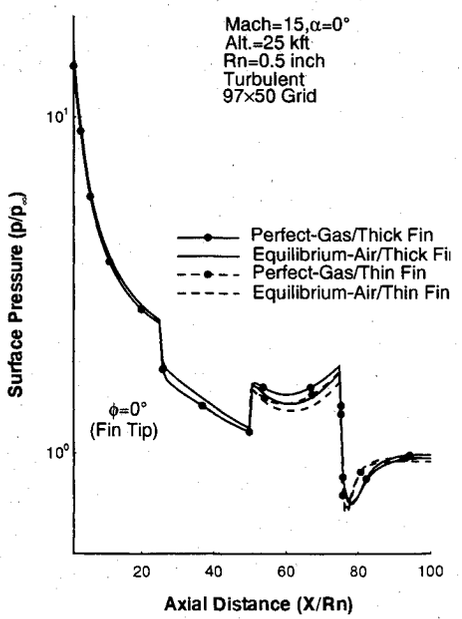

Fig. 6 Axial distribution of surface pressure for case 2 along $\phi = 0$ deg.

of attack, the effects of fins on the normal force, pitching moment, and the center of pressure become even more pronounced (Table 2). In general, these angle-of-attack calculations with a 97×50 grid required approximately 180 marching steps and took less than 23 min on the Cray Y-MP (Table 3).

Figures 8 and 9 show the perfect-gas and equilibrium-air pressure contours for the 5-deg angle-of-attack calculations at axial locations of 65 and 100 *Rn*, respectively. Figure 8 shows a strong embedded shock generated by the leading edge of the fins. For the equilibrium-air case, the embedded shocks are slightly more diffused, and there is a relatively stronger expansion around the side fin. At this axial location, the equilibrium-air shock-layer thickness is uniformly thinner than the perfect-gas case. The corresponding pressure contours at the body end ($x = 100\ Rn$) are shown in Fig. 9. At this location, the equilibrium-air shock-layer thickness on the leeside is, as expected, smaller than the perfect-gas case; however, on the windward side the shock bulges out, and the equilibrium-air shock-layer thickness is more than the perfect-gas prediction. This is because, in the case of the equilibrium-air calculations, the interaction of the fin shock and the bow shock occurs early and, thus, moves the bow shock outward more than the perfect-gas case.

Mach 3 Calculations

For these low Mach number conditions, Fig. 10 shows the computational grids generated at $x = 52.5\ Rn$ using the power-of-4 variation and the power-of-10 variation for the forcing functions [Eqs. (7) and (8)]. Compared with high Mach number flows (cases 2–4), under these low Mach number conditions the shock layer is very thick and the boundary layer is very thin. For such conditions, the power-of-4 law tends to propagate the surface contour and clustering effects much farther into the shock layer, resulting in awkward grid-clustering effects (Fig. 10) that cause the elliptic grid generation (and thus the flowfield solution) to diverge. With a power-of-10 variation (Fig. 10), the surface contour and clustering effects, represented by the forcing functions at the wall [$P_w(\xi_3)$ and $R_w(\xi_3)$ in Eqs. (8)], decay more rapidly, and the shock-conformal grid effects, represented by the forcing functions at the shock [$P_w(\xi_3)$ and $R_s(\xi_3)$ in Eqs. (8)], increase more rapidly. This variation not only produces well-behaved grids, but it also improves the convergence of the flowfield as well as the grid generation.

The pressure contours at the body end with and without side-fin deflection at zero angle of attack are shown in Fig. 11 and show the strong effects of the 5-deg side-fin deflection on the pressure field. As expected, the windward pressures decrease on the deflected fin portion and the leeward pressures increase, resulting in a substantial negative normal force contribution and a significant nose-up pitching moment (Table 2). With fin deflection, the drag increases

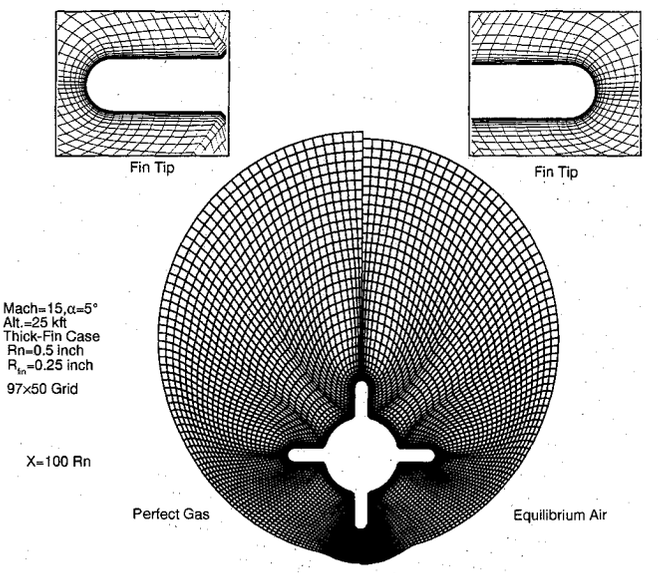

Fig. 7 Computational grid for case 4 at $x = 100\ Rn$.

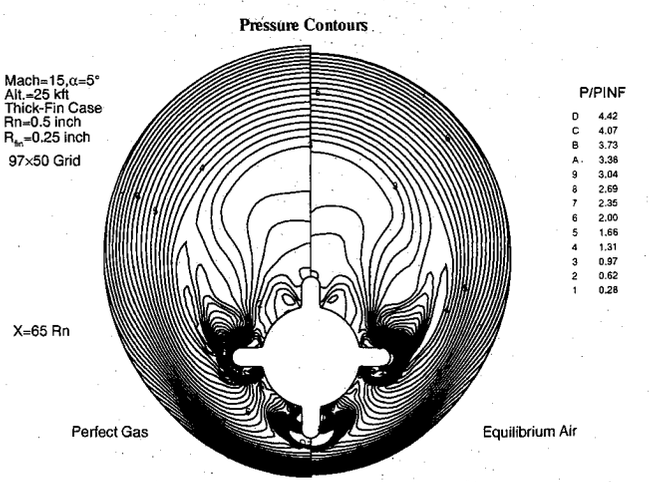

Fig. 8 Crossflow pressure contours for case 4 at $x = 65\ Rn$.

by approximately 5%. The computing times and the computational grids used for these calculations are shown in Table 3.

Calculations for the deflected and undeflected cases were also done at 5-deg angle of attack, and the pressure contours at the body end for these cases (cases 6a and 6b) are shown in Fig. 12. Under these conditions, there is an embedded shock generated by the windward surface of the side fin, and the effects of the flowfield expansion caused by a 5-deg deflection of this side fin are to weaken this embedded shock while causing an increased flowfield compression on the leeside (Fig. 12). In general, there are pronounced effects of the fin deflection on the pressure field around the body. The corresponding temperature contours for these cases are shown in Fig. 13 and show that the fin deflection does not have a pronounced effect on the shock-layer temperature distribution. The effects of fin deflection are limited to the thin boundary-layer region around the fin itself (Fig. 13).

The force and moment data at the body end for these calculations (Table 2) show that there are significant effects of the 5-deg fin deflection on the normal-force and pitching-moment coefficients (16 and 22%, respectively), whereas the effect on the axial-force coefficient is small (1.5%). Compared with the zero angle-of-attack case, in this angle-of-attack case the effect of fin deflection on the axial force is small, because the increased drag due to the increased leeward compression is somewhat offset by the decrease in drag due to the windward expansion effects. Table 2 also shows that, with fin deflection, the pitching moment decreases more rapidly than the normal force. This is because, in this case, the pitching moment decreases not only because of the decreased normal force but also because the upward fin deflection produces an additional nose-up moment. Consequently, with the 5-deg fin deflection, the center-of-pressure location changes by approximately 8%. In short, it is clear that deflectable fin surfaces can substantially change the aerodynamic characteristics of a high-speed missile. This important feature can be used either to augment thruster

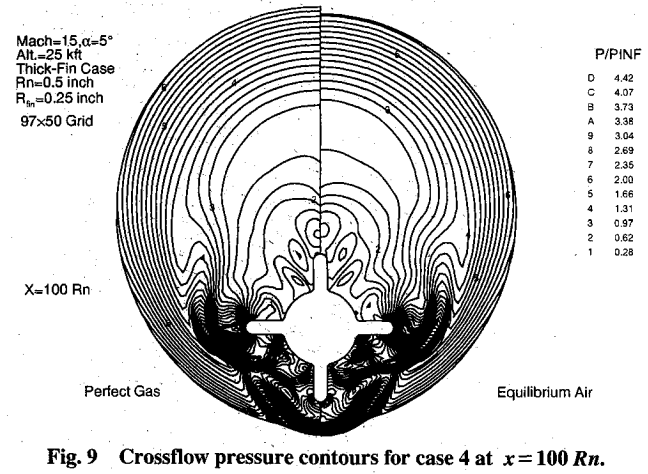

Fig. 9 Crossflow pressure contours for case 4 at $x = 100\ Rn$.

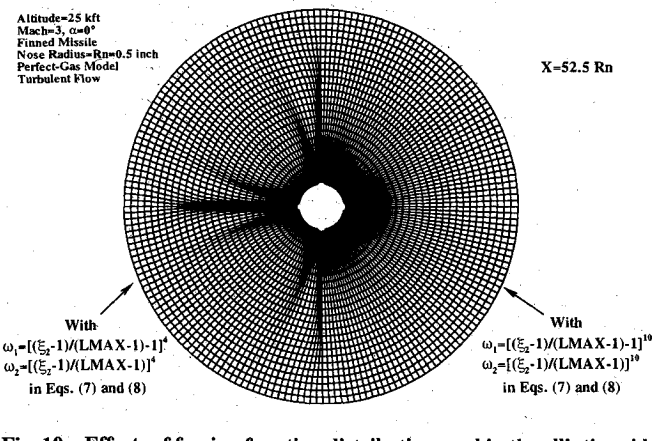

Fig. 10 Effects of forcing function distribution used in the elliptic grid-generation scheme.

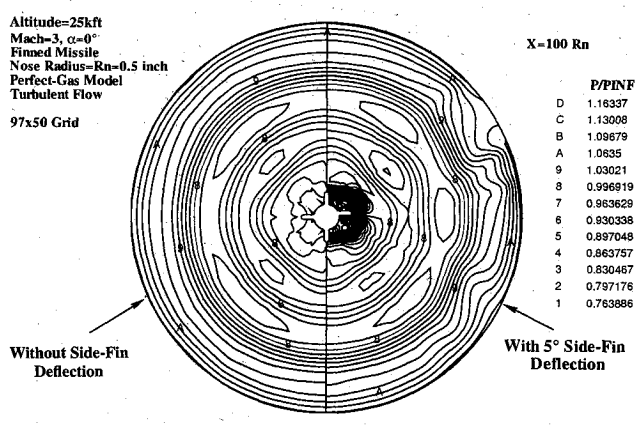

Fig. 11 Comparison of pressure contours at the body end for case 5 with and without side-fin deflection.

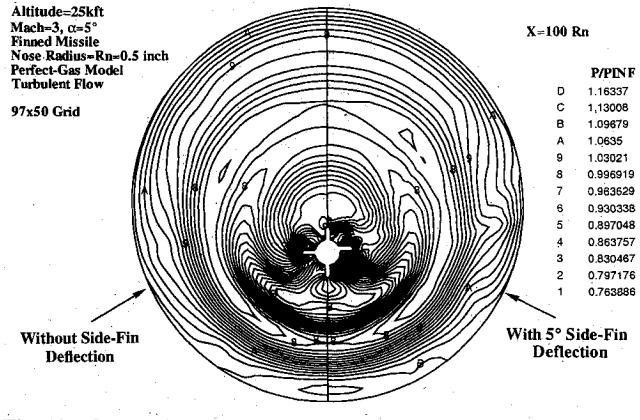

Fig. 12 Comparison of pressure contours at the body end for case 6 with and without side-fin deflection.

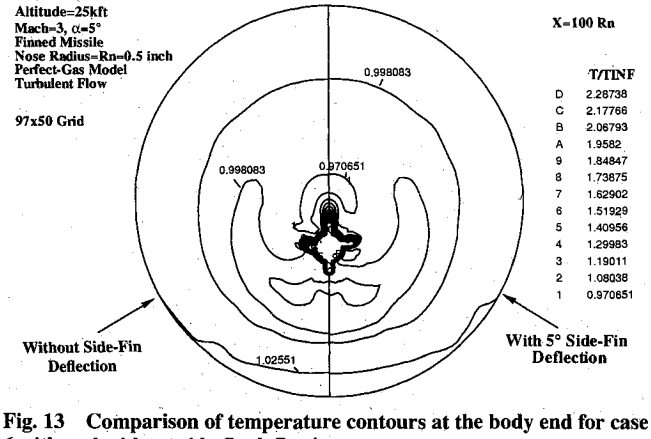

Fig. 13 Comparison of temperature contours at the body end for case 6 with and without side-fin deflection.

action or to lessen the need for using onboard side thrusters or jets used for providing homing and kill maneuverability.[2] Any decreased reliance on thrusters can provide favorable weight and vehicle-guidance characteristics.

The computing times for these angle-of-attack calculations are shown in Table 3 and show that the complete full-body PNS calculation for the undeflected-fin case took approximately 14 min on a Cray Y-MP. The deflected-fin condition increased these computing times by approximately 10%. In general, the computing times required for these calculations are very affordable and encouraging, especially when considering the flowfield complexity.

IV. Conclusions

A new and improved three-dimensional PNS scheme has been developed to treat perfect-gas and equilibrium-air supersonic/

hypersonic flows over complex lifting configurations with fins, flares, and other control surfaces. The improvements consist of including a first-order fully upwind differencing across the embedded shocks and using central differencing in the shock-free flowfield regions. Calculations were made for flows over a 10-deg flare configuration and also a sample finned-missile configuration at zero and nonzero angles of attack. The results of these studies substantiate the following comments:

1) In the absence of strong embedded shocks, the near-wall accuracy of a third-order FVS formulation was not as good as that of a central-differenced approach. A hybrid approach using first-order upwind differencing across embedded shocks and central-differencing otherwise gave the most suitable combination of accuracy, stability, and numerical efficiency.

2) For the conditions tested, the equilibrium-air gas model predicted 20% higher leading-edge heating and 10% lower leading-edge pressure. Furthermore, the shock-layer temperature was lower, the shock layer was thinner, and this thinner shock also affected the subsequent shock-shock interactions. Furthermore, reducing the fin thickness by half resulted in 20% higher leading-edge heating, and the drag was reduced by approximately 4%.

3) Because of the thick shock layers and thin boundary layers under low Mach number (Mach 3) conditions, the elliptic grid-generation schemes designed for higher Mach number flows are inadequate. Appropriate power laws for low and high Mach number flows are given to model the distribution of the forcing functions in the grid-generation equations.

4) Calculations with and without fin deflections at 0- and 5-deg angles of attack show that, under supersonic/hypersonic flow conditions, deflectable fin surfaces can provide a powerful mechanism for augmenting vehicle aerodynamics. The 5-deg angle-of-attack Mach 3 calculations show that, for a relatively small deflection angle of 5 deg, the axial force is only increased by 1.5%, but the normal force and pitching moment decrease by approximately 16 and 22%, respectively, resulting in a net change of 8% in the aerodynamic center of pressure.

Acknowledgments

The work reported in this paper was supported in part by the NASA Lewis Research Center under Contract number NAS3-25450. The encouragement and support provided by Louis Povinelli, Dan Whipple, and the contract monitor Tom Benson, during the course of this effort, are gratefully acknowledged.

References

[1]Dang, A., Tsai, F. P., and Chamberlain, R., "Evaluation of the ATD-GASP for Endo-Leap Applications," AIAA Paper 92-2771, May 1992.

[2]Bischer, G., and Castle, M., "Hypervelocity Gun Projectile Technologies for the D2 Program," AIAA Paper 92-2751, May 1992.

[3]Gierloff, J. J., Robertson, S. J., and Bouska, D. H., "Computer Analysis of Aero-Optic Effects," AIAA Paper 92-2794, May 1992.

[4]Gnoffo, P. A., "Code Calibration in Support of the Aeroassist Flight Experiment," *Journal of Spacecraft and Rockets,* Vol. 27, No. 2, 1990, pp. 131–142.

[5]Walters, R. W., Cinnella, P., Slack, D. C., and Halt, D., "Characteristics-Based Algorithms for Flows in Thermochemical Nonequilibrium," *AIAA Journal,* Vol. 30, No. 5, 1992, pp. 1304–1313.

[6]Schiff, L. B., and Steger, J. L., "Numerical Simulation of Steady Supersonic Viscous Flows," AIAA Paper 79-0130, Jan. 1979.

[7]Kaul, U. K., and Chaussee, D. S., "AFWAL Parabolized Navier-Stokes Code: 1983 AFWAL/NASA Merged Baseline Version," Air Force Flight Dynamics Lab., Air Force Wright Aeronautical Lab., AFWAL-TR-83-3118, Wright-Patterson AFB, OH, Oct. 1983.

[8]Shanks, S. P., Srinivasan, G. R., and Nicolet, W. E., "AFWAL Parabolized Navier-Stokes Code: Formulation and User's-Manual," Air Force Flight Dynamics Lab., Air Force Wright Aeronautical Lab., AFWAL-TR-823034, Wright-Patterson AFB, OH, June 1979.

[9]Murray, A. L., and Lewis, C. H., "Hypersonic Three-Dimensional Viscous Shock-Layer Flows over Blunt Bodies," *AIAA Journal,* Vol. 16, No. 12, 1978, pp. 1279–1286.

[10]Thareja, R. R., Szema, K. Y., and Lewis, C. H., "Chemical Equilibrium Laminar or Turbulent Three-Dimensional Viscous Shock-Layer Flows," *Journal of Spacecraft and Rockets,* Vol. 20, No. 5, 1983, pp. 454–460.

[11]Bhutta, B. A., and Lewis, C. H., "Prediction of Three-Dimensional Hypersonic Flows using a Parabolized Navier-Stokes Scheme," *Journal of Spacecraft and Rockets,* Vol. 26, No. 1, 1989, pp. 4–13; see also AIAA Paper 85-1604, July 1985.

[12]Bhutta, B. A., and Lewis, C. H., "PNS Predictions of Three-Dimensional Hypersonic Flows with Strong Crossflow Effects," *Journal of Thermophysics and Heat Transfer,* Vol. 4, No. 1, 1990, pp. 27–36; see also AIAA Paper 88-2696, June 1988.

[13]Bhutta, B. A., and Lewis, C. H., "Large Angle-of-Attack Viscous Hypersonic Flows over Complex Lifting Configurations," *Journal of Spacecraft and Rockets,* Vol. 27, No. 2, 1990, pp. 194–204; see also AIAA Paper 89-0269, Jan. 1989.

[14]Bhutta, B. A., and Lewis, C. H., "Comparison of Hypersonic Experiments and PNS Predictions, Part I: Aerothermodynamics," *Journal of Spacecraft and Rockets,* Vol. 28, No. 4, 1991, pp. 386; see also AIAA Paper 90-3068, Aug. 1990.

[15]Bhutta, B. A., and Lewis, C. H., "Comparison of Hypersonic Experiments and PNS Predictions, Part II: Aerodynamics," *Journal of Spacecraft and Rockets,* Vol. 28, No. 4, 1991, pp. 387–393; see also AIAA Paper 90-3068, Aug. 1990.

[16]Van Leer, B., "Flux-Vector Splitting for the Euler Equations," NASA Langley Research Center, Inst. for Computer Applications in Science and Engineering, Rept. 82–30, Hampton, VA, Sept. 1982.

[17]Peyert, R., and Viviand, H., "Computations of Viscous Compressible Flows Based on the Navier-Stokes Equations," AGARD-AG-212, 1975.

[18]Steger, J. L., and Warming, R. F., "Flux Vector Splitting of the Inviscid Gasdynamics Equations with Applications to Finite-Differenced Methods," *Journal of Computational Physics,* Vol. 40, No. 2, 1981, pp 263–293.

[19]Sorenson, R. L., and Steger, J. L., "Simplified Clustering of Nonorthogonal Grids Generated by Elliptic Equations," NASA TM-73252, Aug. 1977.

[20]Chaussee, D. S., and Steger, J. L., "Three Dimensional Viscous Flowfield Program; Part 2; A Curvilinear Grid and Body Generation Program for Generalized Configurations (Interim Report)," Flow Simulations Inc., AFWAL-TM-81-64-FIMG, Sunnyvale, CA, March 1981.

[21]Kaul, U. K., and Chaussee, D. S., "A Comparative Study of the Parabolized Navier-Stokes (PNS) Code Using Various Grid Generation Techniques," AIAA Paper 84-0459, Jan. 1984.

Jerry M. Allen
Associate Editor